Gargallo Jaquotot, BA.; Muñoz Muñoz, P.; Baños Lopez, R.; Giesecke, AL.; Bolten, J.; Wahlbrink, T.; Kleinjans, H. (2014). Reflective arrayed waveguide gratings based on Sagnac loop reflectors with custom spectral response. Optics Express. 22(12):14348-14362. doi:10.1364/OE.22.014348.

Reflective arrayed waveguide gratings based on Sagnac loop reflectors with custom spectral response

Bernardo Gargallo,[1,*] **Pascual Muñoz,**[1,2] **Rocío Baños,**[1] **Anna Lena Giesecke,**[3] **Jens Bolten,**[3] **Thorsten Wahlbrink,**[3] **and Herbert Kleinjans**[3]

[1]*Optical and Quantum Communications Group, iTEAM Research Institute Universitat Politècnica de València, C/ Camino de Vera s/n, Valencia 46022, Spain*
[2]*VLC Photonics S.L., C/ Camino de Vera s/n, Valencia 46022, Spain*
[3]*AMO GmbH, Otto-Blumenthal-Straße 25, 52074 Aachen, Germany*

[*]*bergarja@iteam.upv.es*

Abstract: In this paper, a model for the analysis and design of a reflective Arrayed Waveguide Grating is presented. The device consists of one half of a regular AWG where each arm waveguide in the array is terminated with a phase shifter and a Sagnac loop reflector. By individually adjusting the phase shifter and Sagnac reflectivity in each arm, additional functionality to that previously reported in the literature is attained, since this enables tailoring the spectral response of the AWG. The design and experimental demonstration of Gaussian pass-band shape devices in Silicon-on-Insulator technology are reported. Methods to obtain flattened and arbitrary spectral responses are described and supported by simulation results.

OCIS codes: (070.2580) Paraxial wave optics; (130.3120) Integrated optics devices; (130.7408) Wavelength filtering devices; (230.1950) Diffraction gratings.

References and links

1. C.A. Brackett, "Dense wavelength division multiplexing networks: principles and applications," IEEE J. Sel. Areas Commun. **8**(6), 948–964 (1990).
2. R. Kirchain and L. Kimerling, "A roadmap for nanophotonics," Nat. Photon. **1**, 303–305 (2007).
3. E. Pennings, G.D. Khoe, M.K. Smit and T. Staring, "Integrated-optics versus microoptic devices for fiber-optic telecommunication systems: a comparison," IEEE J. Sel. Topics Quantum Electon. **2**(2), 151–164 (1996).
4. M. Smit and C. van Dam, "Phasar-based WDM-devices: principles, design and applications," IEEE J. Sel. Topics Quantum Electron. **2**(2), 236–250 (1996).
5. C. Dragone, "An NxN optical multiplexer using a planar arrangement of two star couplers," IEEE Photon. Technol. Lett. **3**(9), 1041–1135 (1991).
6. C. Dragone, C.A. Edwards, and R.C. Kistler, "Integrated optics NxN multiplexer on silicon," IEEE Photon. Technol. Lett. **3**(10), 896–899 (1991).
7. P. Muñoz, J.D. Domenech, I. Artundo, J.H. den Besten, and J. Capmany, "Evolution of fabless generic photonic integration," in *IEEE 5th International Conference on Transparent Optical Networks (ICTON)* (2013), pp. 1–3.
8. R.J. Lycett, D.F.G. Gallagher, and V.J. Brulis, "Perfect chirped echelle grating wavelength multiplexor: design and optimization," IEEE Photon. J. **5**(2), (2013).
9. D. Feng, W. Qian, H. Liang, C. Kung, J. Fong, B.J. Luff, and M. Asghari, "Fabrication insensitive echelle grating in Silicon-on-Insulator platform," IEEE Photon. Technol. Lett. **23**(5), 284–286 (2011).
10. E. Ryckeboer, A. Gassenq, M. Muneeb, N. Hattasan, S. Pathak, L. Cerutti, J.B. Rodriguez, E. Tournié, W. Bogaerts, R. Baets, and G. Roelkens, "Silicon-on-insulator spectrometers with integrated GaInAsSb photodiodes for wide-band spectroscopy from 1510 to 2300 nm," Opt. Express **21**(5), 6101–6108 (2013).

11. M.W. Pruessner, T.H. Stievater, and W.S. Rabinovich, "Integrated waveguide Fabry-Perot microcavities with silicon/air Bragg mirrors," Opt. Lett. **32**(5), 533–535 (2007).
12. L.G. de Peralta, A.A. Bernussi, S. Frisbie, R. Gale, and H. Temkin, "Reflective arrayed waveguide grating multiplexer," IEEE Photon. Technol. Lett. **15**(10), 1398–1400 (2003).
13. Y. Inoue, A. Himeno, K. Moriwaki, and M. Kawachi, "Silica-based arrayed-waveguide grating circuit as optical splitter/router," Electron. Lett. **31**(9), 726–727 (1995).
14. J.B.D. Soole, M.R. Amersfoort, H.P. LeBlanc, A. Rajhel, C. Caneau, C. Youtsey, and I. Adesida, "Compact polarization independent InP reflective arrayed waveguide grating filter," Electron. Lett. **32**(19), 1769–1771 (1996).
15. D. Dai, X. Fu, Y. Shi, and S. He, "Experimental demonstration of an ultracompact Si-nanowire-based reflective arrayed-waveguide grating (de)multiplexer with photonic crystal reflectors," Opt. Lett. **35**(15), 2594–2596 (2010).
16. L.G. de Peralta, A.A. Bernussi, V. Gorbounov, and H. Temkin, "Temperature insensitive reflective arrayed-waveguide grating multiplexers," IEEE Photon. Technol. Lett. **16**(3), 1041–1135 (2004).
17. K. Okamoto and K. Ishida, "Fabrication of silicon reflection-type arrayed-waveguide gratings with distributed Bragg reflectors," Opt. Lett. **38**(18), 3530–3533 (2013).
18. Y. Ikuma, M. Yasumoto, D. Miyamoto, J. Ito, T. Jiro; H. Tsuda, "Small Helical Reflective Arrayed-Waveguide Grating with Integrated Loop Mirrors," in Proc. European Conference on Optical Communications (ECOC), (2007).
19. K. Okamoto and H. Yamada, "Arrayed-waveguide grating multiplexer with flat spectral response," Opt. Lett.**20**(1), 43–45 (1995).
20. C.R. Doerr, L. Zhang, and P.J. Winzer, "Monolithic InP multiwavelength coherent receiver using a chirped arrayed waveguide grating," J. Lightw. Technol. **29**(4), 536–541 (2011).
21. P. Muñoz, D. Pastor, and J. Capmany, "Modeling and design of arrayed waveguide gratings," J. Lightw. Technol. **20**(4), 661–674 (2002).
22. B.E.A. Saleh and M.C. Teich, "Fundamentals of photonics," in *Wiley Series in Pure and Applied Optics*, B.E.A. Saleh, eds, 2nd ed, (Wiley Interscience, 2007).
23. K. Jinguji, N. Takato, Y. Hida, T. Kitoh, and M. Kawachi, "Two-port optical wavelength circuits composed of cascaded Mach-Zehnder interferometers with point-symmetrical configurations," J. Lightw. Technol. **14**(10), 2301–2310 (1996).
24. L.B. Soldano and E.C.M Pennings, "Optical multi-mode interference devices based on self-imaging: principles and applications," J. Lightw. Technol. **13**(4), 615–627 (1995).
25. M. Bachmann, P. Besse, and H. Melchior, "General self-imaging properties in NxN multimode interference couplers including phase relations," Appl. Opt. **33**(18), 3905–3911 (1994).
26. P.A. Besse, E. Gini, M. Bachmann, and H. Melchior, "New 2x2 and 1x3 multimode interference couplers with free selection of power splitting ratios," J. Lightw. Technol. **14**(10), 2286–2293 (1996).
27. S. Jeong and K. Morito, "Novel optical 90° hybrid consisting of a paired interference based 2x4 MMI coupler, a phase shifter and a 2x2 MMI coupler," J. Lightw. Technol. **28**(9), 1323–1331 (2010).
28. J.W. Goodman, "Introduction to Fourier optics," in *Classic Textbook Reissue Series*, W. Stephen, ed. (New York: McGraw-Hill Higher Education, 1988), Chap. 5, pp. 83–90.
29. H. Takahashi, K. Oda, H. Toba, and Y. Inoue, "Transmission characteristics of arrayed waveguide NxN wavelength multiplexer," J. Lightw. Technol. **13**(3), 447–455 (1995).
30. P. Muñoz, D. Pastor, J. Capmany, D. Ortega, A. Pujol, and J.R. Bonar, "AWG model validation through measurement of fabricated devices," J. Lightw. Technol. **22**(12), 2763–2777 (2004).
31. E. Kleijn, M.K. Smit, and X. Leijtens, "New analytical arrayed waveguide grating model," J. Lightw. Technol. **31**(20), 3309–3314 (2013).
32. W. Bogaerts, P. Dumon, D. van Thourhout, D. Taillaert, P. Jaenen, J. Wouters, S. Beckx, V. Wiaux, and R.G. Baets, "Compact wavelength-selective functions in silicon-on-insulator photonic wires," IEEE J. Sel. Topics Quantum Electron. **12**(6), 1394–1401 (2006).
33. G. Beelen and H.F. Bulthuis, "Arrayed waveguide grating with reduced channel passband asymmetry," Gemfire Corporation, US Patent 7,492,991, (2007).
34. F. Van Laere, T. Claes, J. Schrauwen, S. Scheerlinck, W. Bogaerts, D. Taillaert, L. O'Faolain, D. Van Thourhout, R. Baets, "Compact Focusing Grating Couplers for Silicon-on-Insulator Integrated Circuits," IEEE Photon. Technol. Lett. **19**(23), 1919–1921 (2007).
35. W. Henschel, Y.M. Georgiev and, H. Kurz, "Study of a high contrast process for hydrogen silsesquioxane as a negative tone electron beam resist," J. Vac. Sci. Technol. B **21**(5), 2018–2025 (2003).
36. M.C. Lemme, T. Mollenhauer, H.D.G. Gottlob, W. Henschel, J. Efavi, C. Welch, and H. Kurz, "Highly selective HBr etch process for fabrication of Triple-Gate nano-scale SOI-MOSFETs," Microelec. Eng. **73**, 346–350 (2004).
37. J. Bolten, T. Wahlbrink, N. Koo, H. Kurz, S. Stammberger, U. Hofmann, and N. nal, "Improved CD control and line edge roughness in E-beam lithography through combining proximity effect correction with gray scale techniques," Microelec. Eng. 8710411043 (2010).
38. A. Sakai, T. Fukazawa, and T. Baba, "Estimation of polarization crosstalk at a micro-bend in Si-Photonic wire waveguide," J. Lightw. Technol. **22**(2), 520–525 (2004).

39. E. Kleijn, P. Williams, N. Whitbread, M. Wale, M. Smit, and X. Leijtens, "Sidelobes in the response of arrayed waveguide gratings caused by polarization rotation," Opt. Express **20**(20), 22660–22668 (2012).
40. K. Okamoto and A. Sugita, "Flat spectral response arrayed-waveguide grating multiplexer with parabolic waveguide horns," Electron. Lett. **32**(18), 1661–1662 (1996).
41. P. Muñoz, D. Pastor, and J. Capmany, "Analysis and design of arrayed waveguide gratings with MMI couplers," Opt. Express **9**(7), 328–338 (2001).
42. C.R. Doerr, M.A. Cappuzzo, E.Y. Chen, A. Wong-Foy, L.T. Gomez, and L.L.Buhl, "Wideband arrayed waveguide grating with three low-loss maxima per passband," IEEE Photon. Technol. Lett. **18**(21), 2308–2310 (2006).
43. K. Okamoto, "Fundamentals of optical waveguides," in *Optics and photonics series*, 2nd. ed, (Academic Press, 2005).
44. "Fourier transform pairs", available on-line at http://www.thefouriertransform.com/pairs/fourier.php
45. D.E. Leaird, A.M Weiner, S. Kamei, M. Ishii, A. Sugita, and K. Okamoto, "Generation of flat-topped 500-GHz pulse bursts using loss engineered arrayed waveguide gratings," IEEE Photon. Technol. Lett. **14**(6), 816–818 (2002).

1. Introduction

Wavelength multi/demultiplexers are central components in optical telecommunication networks, and they have been subject of intense research and development since the advent of wavelength-division multiplexing (WDM) in the early 90s [1]. Components for these networks are subject to demanding requirements, both in terms of performance and manufacturing. While performance depends on the particular component, all need to provide stable operation. In terms of manufacturing requirements, a reproducible and mass fabrication process is mandatory. Hence, photonic integration is usually the basis for large count WDM multiplexers. The cost of an integrated circuit is fundamentally related to its footprint [2, 3], and it has a direct impact on the economies of scale for manufacturing, where in general more devices per wafer, i.e. more compact devices, are desired.

Amongst the different implementations for multiplexers, the Arrayed Waveguide Grating (AWG) [4, 5] is one of a few that aligns with the previous statements. Traditionally manufactured on Silica on Silicon integration technology [6], it finds room nearly in all the relevant material platforms, such as Indium Phosphide, Silicon on Insulator, Silicon and Silicon Nitride (for a summary see [7]). The physical layout of an AWG consists of the combination of waveguides and slab couplers [4, 5]. In its most common shape, two slab couplers with input/output waveguides are inter-connected by a set of waveguides, usually referred as arrayed waveguides (AWs). Consecutive waveguides in the array have a length differing a constant amount, which imposes a wavelength-dependent lineal phase front on the signal fed from the first slab coupler. This linear phase front, in combination with the second slab coupler, enable the spatial separation of different wavelengths in different outputs.

In terms of footprint, other integrated multiplexer implementations as the Echelle Diffraction Grating (EDG) achieve considerable size reduction compared to the AWG [8]. The layout of an EDG includes a single slab coupler, with input/output waveguides on one side, and a reflective grating on the opposite end. It is a so-called reflective multi/demultiplexer. One issue with EDGs is to maximize the reflection on the grating, in order to minimize the overall insertion losses, issue which is otherwise not present in a regular AWG. Different approaches exist to increase the reflectivity of the grating in an EDG, the most employed being the deposition of metal layers at the edge of the grating [9], or the addition to the grating of other structures such as Bragg reflectors [10]. While the former supplies broadband reflectors, it requires resorting to additional fabrication steps. Conversely, Bragg reflectors can be manufactured in the same steps that the EDG, but it is well known the reflection bandwidth is inversely proportional to their strength [11].

Similarly, AWG layouts with reflective structures midway in the array, i.e. reflective AWGs (R-AWG) are possible as well. They can have a footprint ideally half of a regular AWG, and

closer to the one of an EDG. Hence, the signals traveling in the arrayed waveguides arrive to the reflectors, and are bounced back to the (single) slab coupler. Although the functionality is the same than in the case of a regular AWG, some additional design considerations are required [12]. The reflectors can be implemented in similar ways to the ones for the EDGs, and the literature shows solutions as reflective coatings on a facet of the chip where the arrayed waveguides end [13, 14], photonic crystals [15], external reflectors [16] and even Bragg reflectors [17] at the end of the arrayed waveguides.

A common issue of all the described approaches for the reflector is that broadband full reflectivity requires additional fabrication steps, and therefore increases the final cost of the multiplexer. In [18] a configuration for a R-AWG, where one Sagnac Loop Reflector (SLR) is used as reflective element at the end of each waveguide in the array, was proposed. A SLR is composed of an optical coupler with two output waveguides, that are connected to each other forming a loop. These reflectors are broadband, can supply total reflection, and can be fabricated in the same lithographic process than the rest of the AWG.

In this paper a theoretical model is developed for the analysis and design of such a R-AWG and validated by means of the measurements of a fabricated device. Furthermore, owing to the fact the reflection of a SLR depends on the coupling constant of the coupler, the methodology to tailor the R-AWG spectral response shape is provided. This is based upon SLRs with different reflectivity for each of the waveguides in the array. The modification of the field pattern in the arrayed waveguides of an AWG allows for spectral response shaping, as for example box like transfer function [19] and multi-channel coherent operations [20] amongst other.

The paper is structured as follows. In Section 2, the theoretical equations describing the full field (amplitude and phase) transfer function of the R-AWG are developed, following the model in [21]. The equations are then particularized the case in which all the SLRs have total reflection, and the AWG response obtained is Gaussian. In Section 3, the equations are used to design and simulate a R-AWG on Silicon-on-Insulator (SOI) technology, and the experimental demonstration of this device is reported as well. Section 4 presents the methodology to obtain flattened and arbitrary spectral reponses, supported by simulations using the model presented. Finally, Section 5 presents the conclusion.

2. R-AWG theoretical model

The schematic view for a reflective AWG (R-AWG) shown in Fig. 1 is used as reference for the equations in this section. As a regular AWG, the layout consists of a group of input and output waveguides connected to one side of the (single) slab coupler. Each of the arrayed waveguides, which are connected to the opposite side of the slab coupler, is terminated with a SLR. The lengths of consecutive waveguides in array differ by a constant amount [4]. The layout in Fig. 1 includes a phase shifter (PS) section in between the waveguides in the array and the SLR, the purpose of which will be detailed later on.

Hence, this configuration allows for adjusting independently the field amplitude and phase in each AW. Though the operation is similar to that of a regular AWG, it is summarized here for completeness. The field introduced through an input waveguide is diffracted in the slab coupler, and collected by the arrayed waveguides on the opposite side. Then the light travels forth and back through each individual and independent AW, PS and SLR. The reflection (amplitude and phase) in each SLR can be different, depending on the coupling constant for the coupler. The overall reflected field reaching back the slab coupler will be diffracted by the AWs. The overall phase relations between AWs will determine the R-AWG behavior. In the most simple case, a constant phase difference between consecutive propagation paths in the array will spatially separate the different wavelengths on the input/output side of the slab coupler.

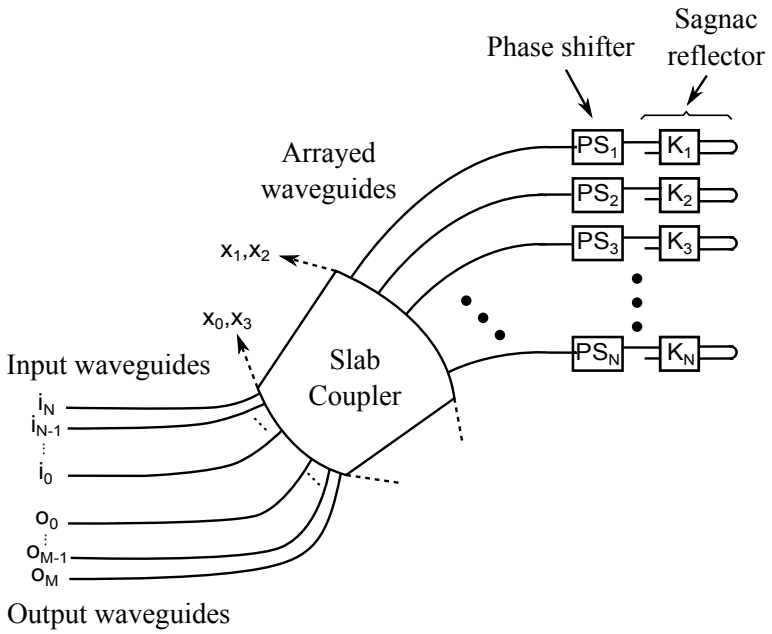

Fig. 1: R-AWG schematic view. Abbreviations: *PS* phase shifter, *K* coupling constant, x_i (i=0,1,2,3) are reference coordinates and i_j, o_j are input and output waveguides, respectively.

2.1. Elements

Though well known, further details are given for the SLR, for which a reference layout is shown in Fig. 2(a). The transfer matrix for the SLR can be expressed as:

$$\begin{pmatrix} o_0 \\ o_1 \end{pmatrix} = \begin{pmatrix} \sqrt{1-k} & j\sqrt{k} \\ j\sqrt{k} & \sqrt{1-k} \end{pmatrix} \begin{pmatrix} i_0 \\ i_1 \end{pmatrix} \tag{1}$$

Hence, it is possible to analyze the SLR as two couplers connected in a series, Fig. 2(b). For the case where only the input i_0 is used, the transfer functions are:

$$o_0' = 2j\sqrt{(1-k)k}e^{-j\beta L}i_0 \tag{2}$$

$$o_1' = (1-2k)e^{-j\beta L}i_0 \tag{3}$$

which at the reproduced the well known total reflection to i_0 when the coupling constant is set to $k = 0.5$. Note that the equations include a phase change due to the length of the loop, L. For coupling constants k other than 0.5, the reflected power will be less than 100%.

The coupler for the SLR can be implemented in multiples ways: directional coupler (DC) [22], wavelength insensitive coupler (WINC) [23] or multimode interference coupler (MMI) [24]. The reflectors for the proposed R-AWG need to be broadband, i.e. the coupling constant needs to be constant over a wide range of wavelengths. Therefore only the WINC and MMI couplers satisfy this condition. Moreover, footprint considerations lead to the selection of MMI vs WINC, since the latter is in general larger than the former. Finally, MMIs can be designed to have arbitrary coupling constant, as described in [25, 26]. Different coupling constants may ultimately result in different MMI lengths/phase shifts.

The purpose of the formerly introduced PS sections is to compensate the phase imbalances between AWs due to different phase shifts/coupling constant/reflection between the SLRs of the

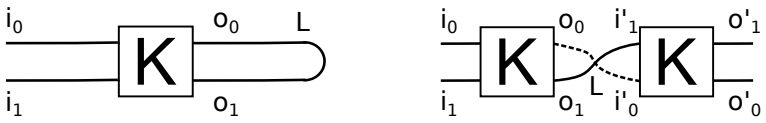

Fig. 2: Sagnac Loop Reflector (a) and SLR analysis as two serial couplers (b). Abbreviations: *i* and *o* stand for input and output waveguides, respectively. *K* stands for coupling constant and *L* stands for loop length.

different AWs. As the coupler, the phase shifter is required to be broadband. This is possible by means of regular straight waveguides, or by tapered waveguides as in [27].

2.2. Principle of operation

The principle of operation for the AWG requires that the phase shift ($\Delta\phi$) between two consecutive AWs is an integer number (m) times of 2π. In the most general case of Fig. 1, the total phase shift the light undergoes in each AW can be given by $\phi_i = \phi_{w,i} + \phi_{PS,i} + \phi_{SLR,i}$, where i is the number of the waveguide and subscripts w, PS and SLR stand for waveguide, Phase Shifter and Sagnac Loop Reflector, respectively. Consider the field in an input waveguide, placed for simplicity at the center input side of the slab coupler, and approximated by the following normalized Gaussian function:

$$b_i(x_0) = \sqrt[4]{\frac{2}{\pi\omega_i^2}} e^{-\left(\frac{x_0}{\omega_i}\right)^2} \tag{4}$$

being ω_i the mode field radius and x_0 the spatial coordinate at the input plane. This field is radiated to the AW side of the slab coupler, where the light spatial distribution can be obtained by the spatial Fourier transform of the input profile, using the paraxial approximation [28]:

$$B_i(x_1) = \mathscr{F}\{b_i(x_0)\}|_{u=\frac{x_1}{\alpha}} = \sqrt[4]{2\pi\frac{\omega_i^2}{\alpha^2}} e^{-(\pi\omega_i(\frac{x_1}{\alpha}))^2} \tag{5}$$

where u is the spatial frequency domain variable of the Fourier transform, x_1 is the spatial coordinate at the AWs plane and α is the equivalent to the wavelength focal length product in Fourier optics propagation, expressed as $\alpha = cL_f/(n_s\nu)$, being L_f the slab length, n_s the effective index of the slab coupler mode, ν the frequency and c the speed of light in vacuum. Note the model can be employed to simulate different modes and polarization by just using the corresponding effective index, e.g. TE or TM. The total field distribution for an arbitrary number N of this way illuminated AWs, placed at the x_1 plane, is [21]:

$$f_1(x_1) = \sqrt[4]{2\pi\omega_g^2}\left[\prod\left(\frac{x_1}{Nd_\omega}\right) B_i(x_1) \sum_{r=-\infty}^{+\infty} \delta(x_1 - rd_\omega)\right] \otimes b_g(x_1) \tag{6}$$

where r is the AW number, d_ω is the spacing, ω_g is the mode field radius, $b_g(x)$ is the field profile of the AWs, $\otimes$ the convolution and $\prod(x_1/Nd_\omega)$ being a truncation function. Let the length of waveguide number r be given by $l_r = l_0/2 + \Delta l/2\,(r + N/2)$, where $l_0/2$ is the (base) length of the shortest waveguide. The value of the incremental length between arrayed waveguides ($\Delta l/2$) is set to an integer multiple m, known as AWG grating order, of the named central design wavelength λ_0, resulting in $\Delta l = m\lambda_0/n_c$, where n_c is the effective index in the waveguides. The value of Δl ensures that the lightwave from a central input waveguide will be focused on

a central output waveguide in a regular AWG for λ_0. The phase shift introduced by waveguide r will be $\Delta\phi_r = \beta l_r = 2\pi n_c \nu l_r / c$, where β is the propagation constant of the (single) mode in the waveguide. As mentioned above, different modes and/or polarizations can be analyzed by setting the corresponding effective index in β. Both the PS and the SLR will introduce an additional phase shift, and the SLR an amplitude change. Hence, the reflected field from the SLRs at the plane x_2, which is the same that the plane x_1 in a R-AWG, is given by:

$$f_2(x_2,\nu) = \sqrt[4]{2\pi\omega_g^2}\left[\prod\left(\frac{x_2}{Nd_\omega}\right) B_i(x_2)\,\phi(x_2,\nu) \sum_{r=-\infty}^{+\infty} \delta(x_2 - rd_\omega)\, e^{-2j\psi_{PS,r}(\nu)}\, jA_r e^{-j\beta l_{SLR,r}}\right] \otimes b_g(x_2) \tag{7}$$

where A_r is the SLRs amplitude term given by $A_r = 2\sqrt{(1-k_r)k_r}$, k_r is the SLR coupling constant, $\psi_{PS,r}(\nu)$ is the phase shift introduced by the PS and $l_{SLR,r}$ is the length of the loop waveguide within the SLR. The phase term $\phi(x_2,\nu)$ is:

$$\phi(x_2,\nu) = \psi(\nu)\, e^{-j2\pi m \frac{\nu}{\nu_0}\frac{x_2}{d_\omega}} \tag{8}$$

$$\psi(\nu) = e^{-j2\pi\nu\left(\frac{n_c l_0}{c} + \frac{mN}{2\nu_0}\right)} \tag{9}$$

The field at the plane x_3 (that is the same that x_0 in a R-AWG) can be calculated using the spatial Fourier transform as:

$$f_3(x_3,\nu) = \mathscr{F}\{f_2(x_2,\nu)\}\big|_{u=\frac{x_3}{\alpha}} \tag{10}$$

Contrary to our previous model in [21] where a closed analytical solution for the field at the output plane is derived, no straightforward closed analytical solution is possible in the general case, due to the arbitrary phase shift for each AW. Nonetheless, the previous equation is the basis for the particular cases derived in the next paragraphs. Independently, the frequency response at the output waveguide q can be calculated through the following overlap integral:

$$t_q(\nu) = \int_{-\infty}^{+\infty} f_3(x_3,\nu)\, b_0(x_3 - qd_o)\, \partial x_3 \tag{11}$$

where d_o is the spacing between, and $b_0(x_3)$ is the field profile of the output waveguides.

2.3. Gaussian spectral response

The basic case for the R-AWG is when all the SLRs are equal and with total reflection, i.e. coupling constant $k = 0.5$. Since the SLRs are ideally identical, no phase shifters are required in this configuration, as reported experimentally in [18]. The layout for this configuration is the same than in Fig. 1, where the phase shifters have been removed, all the SLRs are identical and therefore the length between consecutive AW differ by an incremental length $\Delta l/2$. The equations can be particularized to this case, i.e. Eq. (7) can be rewritten as:

$$f_2(x_2,\nu) = j\sqrt[4]{2\pi\omega_g^2}\, e^{-j\beta l_{SLR}}\left[\prod\left(\frac{x_2}{Nd_\omega}\right) B_i(x_2)\,\phi(x_2,\nu) \sum_{r=-\infty}^{+\infty} \delta(x_2 - rd_\omega)\right] \otimes b_g(x_2) \tag{12}$$

and the field at the output plane (x_3) described using Eq. (10) as:

$$f_3(x_3,\nu) = j\sqrt[4]{2\pi\frac{\omega_g^2}{\alpha^2}}B_g(x_3)\,e^{-j\beta l_{SLR}}\left[b_i(x_3)\otimes \operatorname{sinc}\left(Nd_\omega\frac{x_3}{\alpha}\right)\right.$$
$$\left.\otimes\,\Phi(x_3,\nu)\otimes\sum_{r=-\infty}^{+\infty}\delta\left(x_3 - r\frac{\alpha}{d_\omega}\right)\right] \tag{13}$$

where the different terms therein are given by Fourier transforms as in [21]. Therefore, the field at the output plane can be rewritten as:

$$f_3(x_3,\nu) = j\sqrt[4]{2\pi\frac{\omega_g^2}{\alpha^2}}B_g(x_3)\,e^{-j\beta l_{SLR}}\psi(\nu)\sum_{r=-\infty}^{+\infty} f_M\left(x_3 - r\frac{\alpha}{d_\omega}+\frac{\nu}{\gamma}\right) \tag{14}$$

where $f_M(x_3)$ is defined as $\operatorname{sinc}(Nd_\omega x_3/\alpha)\otimes b_i(x_3)$. Recall during the first steps in the derivation of the model we assumed for simplicity the input waveguide is centered with respect to the slab coupler. Nonetheless Eq. (14) can be readily extended to account for the other input positions, i.e. for the field at the input waveguide number p placed at a distance pd_i from the center position [21], where d_i is the distance between the input waveguides. Then, rewriting Eq. (14):

$$f_{3,p}(x_3,\nu) = j\sqrt[4]{2\pi\frac{\omega_g^2}{\alpha^2}}B_g(x_3)\,e^{-j\beta l_{SLR}}\psi(\nu)\sum_{r=-\infty}^{+\infty} f_M\left(x_3 + pd_i - r\frac{\alpha}{d_\omega}+\frac{\nu}{\gamma}\right) \tag{15}$$

In conclusion, the functionality of the R-AWG and AWG can be described by similar formulation [21]. One important difference in the case of a R-AWG is the positioning of the input/output waveguides, which has implications for the selection of the central design wavelength, however this can be readily accounted for during design as described in [12]. The dispersion angle (θ) with respect to the center of the slab coupler is given by [4]:

$$\theta = \arcsin\left(\frac{\beta\Delta l - m2\pi}{\beta_S d_\omega}\right) \tag{16}$$

where β and β_S are the propagation constants of the AW mode and slab modes, respectively, and d_ω is the spacing between AWs. For the positioning of the input/output waveguides in the R-AWG, the wavelength routing properties of the AWG need to be observed [29]. Let $\lambda_{p,q}$ be the wavelength routed from input p to output q. Changing the input position, for instance to $p-p'$, will route the same $\lambda_{p,q}$ to output $q+q'$, with $p'=q'$ provided the positions of the input/outputs corresponds to the same wavelength displacement given by the derivative of Eq. (16) (see [4]). Fig. 1 shows a layout for N inputs and M outputs, accounting for these routing properties. The central input waveguide $p=0$ is placed a distance to the left from the center of the slab. Therefore, the central output waveguide $q=0$ needs to be placed the same distance to the right from the center.

3. Experimental results

3.1. Design and simulation

In this section, the design cases with transfer function simulation using the equations above (similar to previously validated models [30, 31]) are presented. Despite SLRs can be implemented in nearly all integration technologies [7], the footprint advantage will be so only in

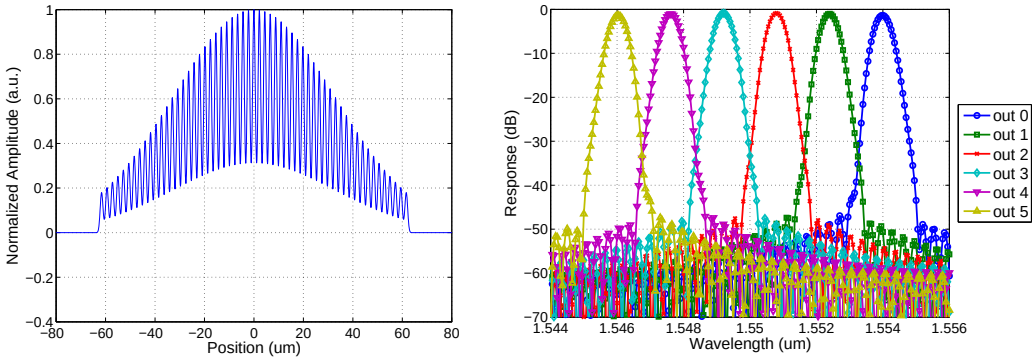

(a) (b)

Fig. 3: Gaussian R-AWG simulation with 1 input and 6 outputs. (a) Field at the arrayed waveguides. (b) Transfer function from i_0 to the output waveguides.

those where the confinement in optical waveguides is strong, i.e. the bend radius can be small. Amongst the different waveguide technologies available, the smallest bend radius is for Silicon-on-Insulator (can be less than 5 μm). Therefore the case provided in the following is for SOI technology, with a 220-nm-thick Si guiding layer on a SiO_2 substrate with no cladding. The effective indexes, calculated using a commercial software, are 2.67 in the arrayed waveguides (n_c) -waveguide with 0.8 μm to minimize phase errors, see [32]- and 2.83 in the slab coupler (n_s) for TE polarization. All the subsequent simulation results are for TE polarization. For TM, the corresponding indices had to be used and analog simulations performed. Note the fact most of the SOI chips employ grating couplers as light input/output structures to/from the chip, and they support only a single polarization.

The R-AWG parameters are the following: the center wavelength is 1550 nm, using 6 channels with a spacing of 1.6 nm and a FSR of 19.2 nm. The calculated focal length is 217.37 μm, the incremental length between AWs is 31.38 μm and the number of AWs is 57. The bend radius was set to 5 μm, and the SLR loop length was set to a circumference of that radius, 31.4 μm. The design makes use of a single input waveguide i_0 placed at the center position of the slab coupler input/output side. Consequently, the output waveguides are divided in two halves, each at one different side of the input waveguide. This will result into a wavelength displacement of half channel (0.8 nm) in the output spectra, with respect to the design wavelength [29]. The motivation to use this special input/output configuration is given by the fact a Rowland mounting is used as input/output plane. In the case the input waveguide is displaced from the center, additional fine tuning techniques are required to compensate for the non-uniformities that arise, for example the modification of the angle and position for the waveguides as described in [33].

The transfer function was computed for a Gaussian response R-AWG device. As described in Section 2.3, the layout does not need and all SLRs need to have identical coupling constant $k = 0.5$, for total reflection. Fig. 3(a) shows the Gaussian field distribution at the plane x_2 obtained as the summation of all the AW contributions through Eq. (12). The corresponding end-to-end transfer function for this R-AWG is depicted in Fig. 3(b).

Note the simulations show losses of approximately 1 dB for the central channel and lower than 1.5 dB for the side channels. We did not include the propagation loss in the waveguides for SOI (typically around 4 dB/cm) and other detrimental effects as fabrication imperfections. The actual peak insertion loss of a regular SOI AWG can be as low as 4-5 dB. From the simulation

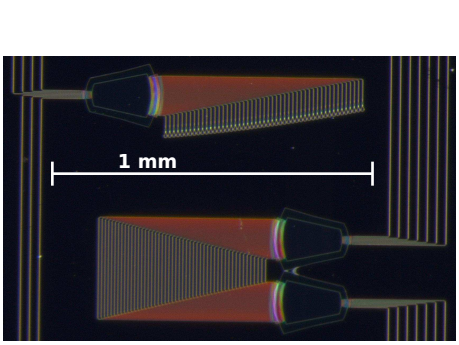

(a) Optical microscope image of the fabricated devices

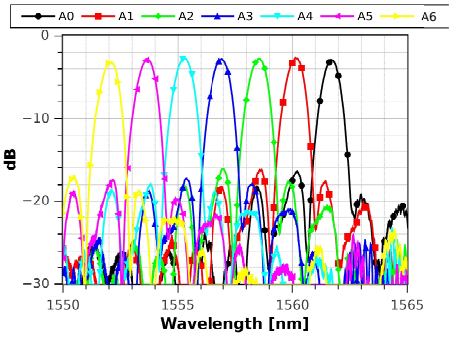

(b) AWG spectra

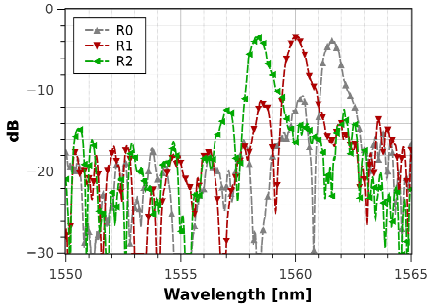

(c) R-AWG spectra

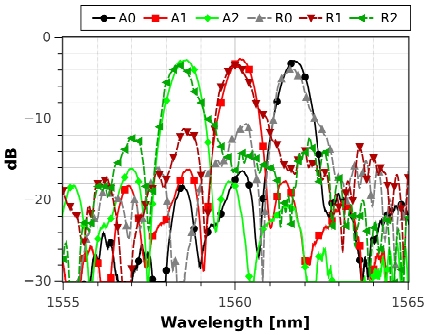

(d) Comparison R-AWG vs AWG

Fig. 4: Optical microscope image of the fabricated AWGs (a) and spectral traces, (b) regular AWG, (c) R-AWG and (d) comparison.

the 1-dB, 3-dB and 20-dB bandwidths are 0.28 nm, 0.49 nm and 1.24 nm respectively.

3.2. Device fabrication and characterization

Following this model and methodology, regular and reflective AWGs were designed having as target polarization TE on SOI substrates. The R-AWG parameters for the manufactured devices are: center wavelength 1550 nm, 7 channels with spacing 1.6 nm and free spectral range of 22.4 nm, focal length 189.32 μm, length increment 36.03 μm and the number of arms is 49. The R-AWG footprint is 350x950 μm^2 (width x height) following the orthogonal layout of Fig. 1. The fabricated devices are shown in Fig. 4(a). Each waveguide in the R-AWG array is terminated by a SLR built with a 1x2 Multimode Interference coupler [24], with 50:50 splitting ratio for ideally full reflectivity. The input/output waveguides are equipped with focusing grating couplers (FGCs) [34].

The waveguides are fabricated on the SOI substrates by Electron Beam Lithography (EBL) and dry etching in a two-step process. First, using hydrogen silsesquioxane negative tone resist in combination with a high contrast development process [35] all device features are defined and fully etched to the buried oxide using an HBr-based ICP-RIE process [36]. In a second step, a positive tone ZEP resist mask is carefully aligned to those features, exposed and used to define the shallow etched parts of the devices using a C4F8/SF6-based dry etching process. For both process steps a multi pass exposure approach is used to further reduce the sidewall roughness of

the photonic device, hence minimizing scattering losses in those devices. Furthermore, special care is taken to guarantee accurate critical dimensions of all parts of the device by applying a very accurate proximity effect correction in combination with a well-balanced exposure dose [37].

For spectral characterization, a broadband source was employed in the range of 1525-1575 nm, and traces were recorded using a Optical Spectrum Analyzer with 10 pm resolution. All the traces were normalized with respect to a straight waveguide. The results are shown in Fig. 4. Panel (b) shows the spectra for the seven channels of the AWG, from the central input. The peak insertion loss is approximately 3 dB. Note this value is subject to small variations in the performance of the FGCs (expected $\pm$ 0.4 dB). The highest side lobe level is 12 dB below the pass band maximum. The presence of these relatively high side lobes may be attributed in part to the multimode nature of the straight sections, of width 800 nm, in the array. Besides, other detrimental effect may be polarization rotation in the bends. All the bends had a width of 450 nm, and despite some simulation studies [38] state polarization rotation is negligible for this waveguide width and the radius employed (5 μm), they did not take into account slanted waveguide walls (as for instance in [39]).

The spectra for the three inner channels of the R-AWG, from the central input, is shown in Fig. 4(c). The other three channels were not designed to be measured, as they end in the same side of the chip than the central input. Finally, Fig. 4(d) shows the comparison of both AWG and R-AWG. Two main differences are clearly visible in the figure, between the AWG and the R-AWG. These can be seen in (d) comparing for instance traces A0 and R0. First, the shape of the pass band is slightly degraded towards longer wavelength, for the R-AWG, where broadening happens at 6 dB below maximum. Second, the side lobe level is increased by 4 dB in the R-AWG as compared to the AWG. Being the only difference between both devices the presence of SLRs, these degradations are likely to be due to phase/amplitude imperfections in the reflectors. Furthermore, note the light in each arm of the R-AWG, compared to the AWG, travels through one extra curved section, the loop back waveguide in the SLR, and additional polarization rotation may take place.

4. Outlook: flattened and arbitrary spectral responses

4.1. Flattened response

There are different techniques to flatten the spectral response of an AWG, amongst them the use of parabolic waveguide horns [40], MMIs [41] and interferometers [42] at the input/output waveguides. Other technique proposes the modification of the amplitude and phase in the AWs to obtain a sinc field profile [19]. The latter builds upon the signal theory duality between fields at both sides of the slab coupler, through the (spatial) Fourier transform. To obtain a box like field pattern at the output side of the slab coupler, through the diffracted (the Fourier transform) field, a sinc distribution is required in the AWs [19, 43]. As mentioned in the introduction, the SLR based R-AWG layout allows for the modification of the phase front by means of the phase shifters, while the amplitude can be adjusted by means of the SLRs. Recall the Fourier transform of a Π function is:

$$\mathscr{F}\left\{\prod\left(\frac{x}{A}\right)\right\}\Big|_{u=\frac{y}{\alpha}} = A\text{sinc}\left(A\frac{y}{\alpha}\right) \tag{17}$$

where A is the rectangular width, and x, y the spatial variables. Therefore, the field at the plane x_2 will be modified to adjust it to a sinc function as described in [43]. In the formulation, the adjustment can be incorporated by the terms in Eq. (7), to be precise $2j\sqrt{(1-k_r)k_r}e^{-j2\psi_{PS,r}(\nu)}e^{-j\beta l_{SLR,r}(\nu)}$, from which the following amplitude and phase conditions are derived to turn the input far field Gaussian profile $B_i(x_2)$ into a sinc function. Hence,

the amplitude condition is written as follows:

$$B_i\left(rd_w\right)\sqrt{\left(1-k_r\right)k_r}=\left|\mathrm{sinc}\left(ard_\omega/\alpha\right)\right| \tag{18}$$

where a will be the obtained rectangular function width when using the Fourier transform, as is detailed below. In addition, the following phase condition is required to turn the all positive values from the input far field Gaussian into negative (π shift) where needed:

$$2\psi_{PS,r}\left(\nu\right)+\beta l_{SLR,r}=\begin{cases}0, & \text{if } \frac{2n\alpha}{a}\leq\left|rd_\omega\right|\leq\frac{(2n+1)\alpha}{a} \quad \text{with n=0,1,...}\\ \pi, & \text{otherwise}\end{cases} \tag{19}$$

Under these conditions, the sinc field profile for the AWs can be introduced in Eq. (7) for x_2, resulting in:

$$f_2\left(x_2,\nu\right)=j\sqrt[4]{2\pi\omega_g^2}\left[\prod\left(\frac{x_2}{Nd_\omega}\right)B_i\left(x_2\right)\phi\left(x_2,\nu\right)\sum_{r=-\infty}^{+\infty}\delta\left(x_2-rd_\omega\right)\mathrm{sinc}\left(a\frac{rd_\omega}{\alpha}\right)\right]\otimes b_g\left(x_2\right) \tag{20}$$

Finally, the field at the plane x_3 calculated through the spatial Fourier transform of Eq. (20) is given by:

$$f_{3,p}\left(x_3,\nu\right)=j\sqrt[4]{2\pi\frac{\omega_g^2}{\alpha^2}}B_g\left(x_3\right)\psi\left(\nu\right)\sum_{r=-\infty}^{+\infty}f'_M\left(x_3+pd_i-r\frac{\alpha}{d_\omega}+\frac{\nu}{\gamma}\right) \tag{21}$$

where $f'_M\left(x_3\right)$ is in this case:

$$f'_M\left(x_3\right)=\mathrm{sinc}\left(Nd_\omega x_3/\alpha\right)\otimes\left(\alpha/a\right)\prod\left(x_3/a\right) \tag{22}$$

Eq. (22) describes the field shape at the output plane, being the second term in the equation the obtained rectangular profile from the sinc field distribution in the AWs. In general, there is a trade-off between the desired channel flatness and the acceptable channel width increase, which is inversely proportional to the number of zeros of the sinc field distribution in the AWs. Furthermore, the use of a more "compressed" sinc will reduce the amplitude of the obtained dual rectangular function, i.e. the AWG will have a flatter response, but with more peak insertion loss.

Using the same physical parameters as in Section 3.1, but for a R-AWG with sinc field distribution in the AWs, the transfer function is computed resulting in a flattened spectral response. A sinc profile with a = 3.5 μm is incorporated. From this distribution, the required coupling constant k_r for each SLR is calculated using Eq. (18). Note the use of a different coupler in each AW may introduce a different phase shift in each arm [26], as already mentioned. For simplicity, this phase shift has not been included in Eq. (19) since it can be compensated through the phase shifters. Fig 5(a) shows the field distribution at the plane x_2, being this field the summation of all the AW contributions in blue trace. On the same figure, the sinc function applied is shown in green line. Moreover, the secondary axis shows in red crosses the required coupling constant for each SLR to obtain the sinc profile.

As described above, to obtain a wider rectangular function, a more compressed sinc function at the AWs is required. However, widening comes at the expense of increased channel insertion loss. This can also be understood by comparing Fig. 3(a) and Fig 5(a), from which is clear the sinc field distribution is attained in part by modifying the amplitude of the original Gaussian field distribution, with partial reflectors, i.e. some signal is lost. The transfer function for the flat-top R-AWG is shown in Fig. 5(b). The flat spectral response and increased insertion losses are clearly noticeable by comparing these results with Fig. 3(b). The obtained losses in this

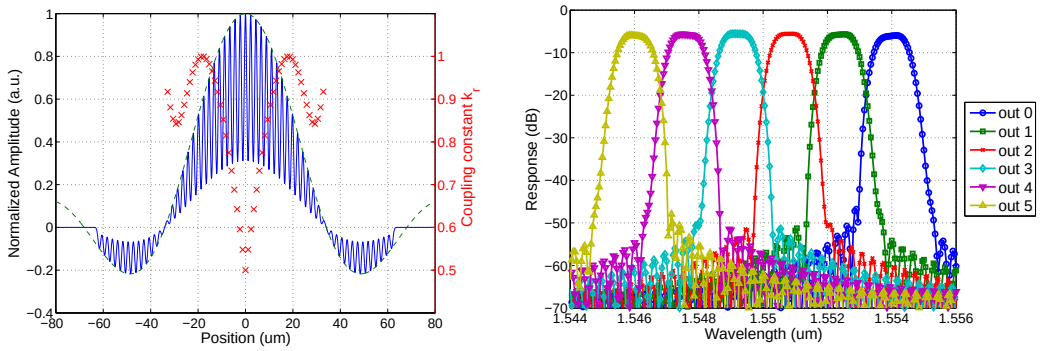

(a) (b)

Fig. 5: Flat-top R-AWG using a sinc field distribution at the arrayed waveguides. (a) Field at the arrayed waveguides (blue solid), the sinc profile applied (green dashed) and SLR coupling constant k_r in each arm of the array (red crosses). (b) Transfer function from i_0 to the output waveguides. (Both for a sinc distribution with parameter a=3.5μm).

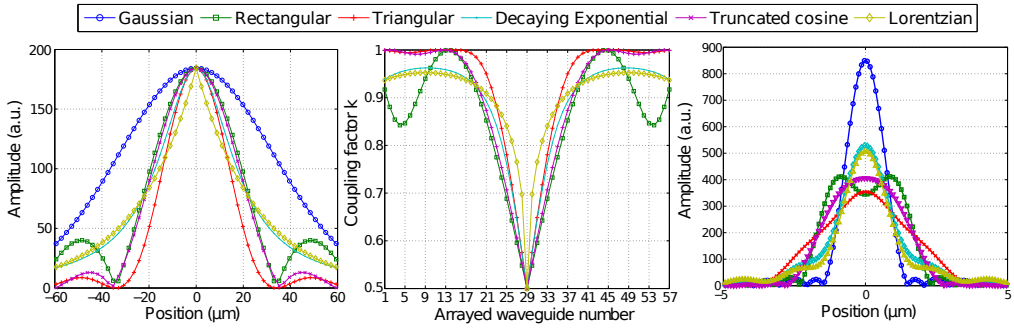

(a) (b) (c)

Fig. 6: Field focused at the output plane when using the central wavelength (λ_0) for each different profile applied at the AWs.

case are 5.6 dB and 6.2 dB for the central and side channels respectively. The bandwidths at the points of interest are in this case 0.76 nm, 1.02 nm and 1.78 nm, for 1-dB, 3-dB and 20-dB fall from the channel center. As expected, an increase in the channel bandwidth is attained at the expense of more insertion losses. Note the closer these values are, the better (more box shapped) is the response. At the sight of all the above, a variation of the sinc field distribution in the AWs may be found numerically to that purpose. Finally, the lateral channels shape appears slightly degraded compared to the central channels. This can be corrected by optimizing its positions with respect to the canonical Rowland circle, as described in [33].

4.2. Arbitrary spectral responses

Although the semi-analytical model in previous sections was only derived for the Gaussian and flattened response cases, in principle it is possible to apply any desired field distribution for the AWs, which will result in different spectral responses. In this subsection we present several field

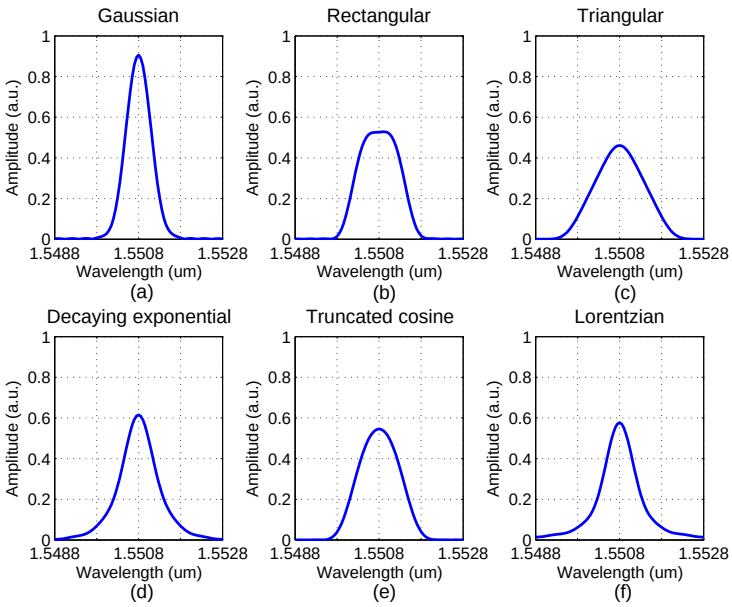

Fig. 7: Transfer function (linear) in one output waveguide for each different profile applied: (a) Gaussian, (b) rectangular, (c) triangular, (d) decaying exponential, (e) truncated cosine and (f) Lorentzian functions.

distributions and corresponding spectral responses, which we take from well-known Fourier transform pairs. To be precise, we targeted triangular, decaying exponential, truncated cosine and Lorentzian spectral responses. The mathematical expressions for these functions are listed in Table 1. Hence, Fig. 6(a) shows the required AWs field distributions, i.e. at plane x_2. Note the legend labels are for the target transform pair, not the actual function employed in the field distribution for the AWs. Detailed expressions can be found elsewhere, as for instance in [44].

Similar to the previously shown case for the flattened response (AWs sinc distribution), the required coupling factors k to be applied in each AW are shown in Fig. 6(b). Note there is no plotted value for the Gaussian case, since all the SLRs use $k = 0.5$ for full reflection. An additional important remark is how the regular Gaussian field distribution ingoing to the array is transformed into the targeted one. In principle some field distributions, can have amplitudes higher than those of the Gaussian for some of the waveguides in the array. This would require amplification, which is not contemplated with the proposed SLR-based layout. Therefore, the targeted profile needs to be inscribed under the starting Gaussian profile. Hence, the amplitude in each AW needs to be reduced to inscribe the profile inside the Gaussian, at the cost of more insertion losses. This is the result in Fig. 6(a), where all the field profiles at the AWs have amplitude levels below the starting Gaussian distribution.

The flat spectral response case, developed in Section 4.1, shows the shape of the field at the output plane given by Eq. (22). For all the targeted spectral responses, this far field at the output plane is plotted in Fig. 6(c) for λ_0. The far field is not exactly the Fourier transform pair of the AWs field distribution in Fig. 6(a). As expressed in Eq. (22), the field profiles at x_2 have a finite extensions (i.e. a finite number of AWs is employed), therefore the field profiles are truncated and the far field is in fact the convolution between a sinc function (Fourier transform of a truncation function in the array) and the Fourier transform of the profile applied at the AWs. From all the curves in Fig. 6(c) the triangular function case (red line) is the most suitable

to understand this fact. Ideally, for an infinity (unpractical) number of AWs, one would expect a perfect (sharp) triangular shape, but in practice the truncation by a finite number of waveguides results in some smoothing in the curves.

Function	Target output response	AWs field distribution	a in simulations
Rectangular	$\prod(x/a)$	$a\mathrm{sinc}(ay)$	3.5 μm
Triangular	$\Lambda(x/a)$	$a^2\mathrm{sinc}^2(ay)$	3.5 μm
Decaying exponential	$e^{-\lvert ax\rvert}$	$2\lvert a\rvert / \left(\lvert a\rvert^2 + (2\pi y)^2\right)$	0.5 μm
Truncated cosine	$\cos\left(\frac{\pi x}{a}\right)\prod\left(\frac{x}{a}\right)$	$\frac{a}{2\pi}\left[\frac{\cos(\pi ya)}{\left(\frac{1}{2}\right)^2-(ya)^2}\right]$	5 μm
Lorentzian	$\frac{1}{\pi}\frac{0.5a}{x^2+(0.5a)^2}$	$e^{-a\pi\lvert y\rvert}$	1.5 μm

Table 1: Mathematical Fourier transform pair expressions.

In addition to this intrinsic smoothing, the corresponding end-to-end transfer functions for the R-AWGs involves the calculation of the convolution integral between the (already smoothed) far field at the output plane and the mode at the output waveguide, as described by Eq. (11). The transfer functions are depicted in Fig. 7, using linear units, for the output waveguide o_2, placed at a distance 2.24 μm from the slab center.

5. Conclusion

This paper proposes a model for a type of reflective Arrayed Waveguide Grating, that makes use of a configuration based on phase shifters and Sagnac Loop Reflectors, built with an optical coupler with loop back waveguides. The layout enables the control of the field amplitude and phase per arm in the array, with the combination of phase shifters and SLRs whose reflectivity is set through the coupling constant of the optical coupler. A theoretical model for the analysis and design of the device has been provided, both for the cases of Gaussian and flattened response, the latter achieved by adjusting the AW field distribution to a sinc function by means of the SLRs and phase shifters. The model was used to design and simulate Silicon-on-Insulator implementations using typical waveguide cross-sections for the technology. This was presented for the Gaussian and flattened spectral response cases, as well as for different field distributions in the AWG arms that result in principle with an arbitrarily customizable spectral response. The first experimental demonstration on Silicon-on-Insulator technology for such a R-AWG layout is also reported. We believe profiles in the AWs can be found to pre-equalize the intrinsic spectral response smoothings described, in order to obtain closer to target spectral responses. The processing of photonic signals in the wavelength domain, i.e. multi-wavelength spectral filtering/shaping, is just one of the possible applications of this versatile R-AWG layout. We envisage more applications for which the field distribution in the AWs is determinant, as the use of AWGs for pulse rate multiplication, where the envelope of the train of pulses generated by the AWGs is directly dictated by the field distribution in the arms [45].

Acknowledgment

The authors acknowledge financial support by the Spanish MINECO projects TEC2010-21337, TEC2013-42332-P; FEDER UPVOV 10-3E-492 and UPVOV 08-3E-008. B. Gargallo acknowledges financial support through FPI grant BES-2011-046100. The authors thank J.S. Fandiño for helpful discussions.